Research Square

Preprints are preliminary reports that have not undergone peer review.
They should not be considered conclusive, used to inform clinical practice,
or referenced by the media as validated information.

Robotic Additive Manufacturing of Aligned Long Discontinuous Carbon-Fiber Thermoset Composites

Ji Ho Jeon
jiho.jeon@uconn.edu

University of Connecticut https://orcid.org/0009-0009-2182-1063
Akshay Zaveri
University of Connecticut
Kisu Ok
University of Connecticut
Minhajul Islam
University of Connecticut
Cheonghwa Lee
KUMOH NATIONAL INSTITUTE OF TECHNOLOGY
Omar Bhatti
University of Connecticut
Jack Heroux
University of Connecticut
Jaeyoul Lee
Korea Institute of Robotics & Technology Convergence

Article

Keywords: aligned discontinuous fiber composites, additive manufacturing, carbon fiber, long-fiber deposition, thermoset composites, UV/thermal dual cure

Posted Date: May 14th, 2026

DOI: https://doi.org/10.21203/rs.3.rs-9694624/v1

License: This work is licensed under a Creative Commons Attribution 4.0 International License. Read Full License

Additional Declarations: Yes there is potential Competing Interest. The authors declare the following competing interests: The University of Connecticut has filed U.S. Provisional Patent Application No. 64/049,520, titled “Robotic Additive Manufacturing System and End Effector for Aligned Long Discontinuous Fiber Composites,” related to the direct additive manufacturing process and deposition-head architecture described in this manuscript. Ji Ho Jeon, Minhajul Islam, Akshay Zaveri, Kisu Ok and Cheonghwa Lee are listed as inventors on the application. The application is pending. All other authors declare no competing interests.

Abstract

Aligned long discontinuous fiber composites provide a reinforcement architecture for geometries in which continuous tow or tape placement is constrained by tight curvature, tow waviness and edge-length mismatch. Here we develop and experimentally demonstrate a compact direct additive manufacturing process using a purpose-built 420 cm³ robotic deposition head, which converts dry continuous carbon fiber tow and an uncured thermoset resin system into aligned long discontinuous composite paths at the point of deposition. The integrated system combines tow chopping, doctor-blade resin metering, in situ impregnation, alignment, compaction and UV-triggered snap cure, eliminating separate tape making, suspension alignment, vacuum collection and preform preparation. By prescribing the start and end positions of 50 mm resin-impregnated tow segments, the process places reinforcement through sharp bends, 90° corners and thin-walled truss geometries while preserving programmed fiber trajectories. A dual UV/thermal formulation with 0.25 wt% tert-butyl peroxybenzoate stabilizes deposited paths and improves cure completion after thermal post-cure. Printed composites achieve 99% tow alignment within ± 2.58°, 28 ± 2.2% fiber volume fraction and 529.1 ± 40.1 MPa tensile strength, demonstrating a functional hardware implementation for direct manufacturing of complex aligned long discontinuous carbon fiber composites.

1. Introduction

High demand for lightweight, high-strength structures has accelerated implementation of continuous fiber reinforced composites (CFRCs). Robotic processes such as filament winding and automated fiber placement (AFP) reduce labor content and variability but still depend on high-precision equipment and energy-intensive consolidation and curing, leading to higher cost and energy use than high-throughput discontinuous fiber composite processing methods [1, 2].

This motivates interest in discontinuous fiber reinforced composites (DFRCs), particularly aligned discontinuous fiber reinforced composites (ADFRCs), which can retain much of the mechanical performance of continuous-fiber systems while offering improved processability and formability [3, 4]. Prior analytical and experimental studies have also shown that longer aligned fibers improve mechanical performance. However, existing alignment methods are often slow, expensive, and limited in fiber length, typically relying on carrier-fluid, vacuum-drum, or electrostatic approaches [4, 5]. The most widely used methods, such as HiPerDiF, produce highly aligned short-fiber tapes, but do so through a multi-step suspension, conveyance, and vacuum-based process [4, 6]. More broadly, many existing ADFRC manufacturing approaches ultimately generate tape-like or semi-discontinuous feedstocks, in which fiber ends are staggered such that partial continuity is retained along the deposition path. Although these feedstocks improve formability relative to conventional continuous-fiber prepregs, they remain constrained by tape-steering and forming limits, where inner- and outer-edge path-length mismatches can introduce defects such as buckling, pull-up, and folding at tight radii [7].

These limitations become even more restrictive for thin-walled, hollow, or lattice-like composite structures, where structural efficiency is high but manufacturing remains challenging [8–10]. More broadly, industrial uptake of DFRCs and ADFRCs has remained limited by the lack of scalable, robot-compatible, and scalable robotic manufacturing platforms compatible with in situ process monitoring and feedback control [2, 4].

Here, we report, to the authors' knowledge, the first compact robotic end effector that performs carbon-fiber tow chopping, thermoset resin impregnation, alignment, deposition, compaction, and UV-assisted fixation in situ within a single 420 cm^3 tool. Unlike prior ADFRC approaches that first create aligned tapes, preforms, or semi-discontinuous feedstocks before placement, this system converts dry continuous tow and liquid resin directly into deposited aligned discontinuous composite paths during printing. This integration reduces equipment complexity, eliminates intermediate feedstock preparation, and enables sharp-angled corners and locally varying paths that are difficult to realize using continuous or semi-discontinuous systems. The system enables deposition of 50 mm fibers with 99% of tows aligned within ± 2.58°, while also offering greater geometric freedom for corners, short-radius bends, and other locally varying paths that are difficult to achieve with conventional tape-based methods. We present the system architecture and evaluate its resin formulation, cure behavior, alignment quality, constituent content, and mechanical performance.

2. Results

2.1. Integrated Chopping, Impregnation, Alignment, and Deposition of Long Carbon Fiber Tows

A gantry-based long-fiber additive deposition system was developed to manufacture highly aligned long discontinuous fiber composites directly from raw carbon fiber tow feedstock. The central advance of the system is a compact end effector that integrates operations that are typically separated across multiple processing stages: tow feeding, fiber chopping, resin impregnation, deposition, compaction, and UV-assisted fixation. As a result, the tool does not require pre-impregnated tow, pre-aligned discontinuous fiber tape, carrier-fluid alignment, vacuum collection, or a separate tape-making process. Instead, dry continuous tow and liquid resin are converted directly into deposited aligned discontinuous composite paths at the point of manufacture.

Raw tow feedstock passes through four sequential operations as shown in Fig. 1(a) First, the tow passes through a feed roller and is chopped to 50 mm lengths by a chopper roller [11]. Second, chopped tows are pulled through doctor-blade rollers and coated with resin [12]. Third, the impregnated tows are deposited on the print bed. Finally, a compaction roller holds fibers in place and removes excess resin while UV light cures the resin sufficiently to fix the deposited tow trajectory. Completed specimens are then thermally cured.

This architecture is distinct from tape-based ADFRC manufacturing because a fully discontinuous architecture is generated at the end effector rather than upstream in a separate feedstock-production step. Consequently, the deposited material does not retain the same edge-continuity constraints as continuous or semi-discontinuous tapes, allowing the toolpath to accommodate sharper bends without tape stretching, shearing, or wrinkling as shown in Fig. 1(c-e).

2.2. Dual UV/Thermal Cure Formulation for Carbon-Fiber-Rich Regions

A UV-curable resin was incorporated to provide rapid in situ snap-cure during deposition, increasing the viscosity and stiffness of the resin sufficiently to preserve the programmed tow trajectory before thermal post-cure. This requirement creates a cure-depth challenge in carbon-fiber composites: high conversion is needed for tensile strength and fiber–matrix load transfer, but carbon fibers attenuate incident UV light and restrict cure within impregnated tow bundles [13, 14]. Although high cure has been demonstrated in thin UV-cured fiber composites, thicker or wider filaments reduce UV transmission and can leave under-cured regions [14].

Prior hybrid UV/thermal systems address the need for rapid shape retention during printing, but separated cure mechanisms can still leave shadowed residual resin or produce resin-rich interlayers that weaken inter-tow load transfer, particularly in discontinuous fiber architectures where stress transfer occurs across tow ends and tow-matrix interfaces [13, 15]. We therefore used a dual-cure strategy in which a thermal initiator (TI) is added directly to the UV resin formulation. UV exposure stabilizes the deposited tow path during printing, while subsequent heating activates thermally generated radicals to advance cure in region that receive insufficient UV intensity [16, 17]. This approach couples deposition stability with cure completion in carbon-fiber-rich regions, addressing a central materials-processing challenge in photocurable composite additive manufacturing.

In this study, tert-butyl peroxybenzoate (TBPB) was selected as the thermal initiator for the UV-curable resin [18]. However, TBPB also introduces processing challenges, since its exothermic decomposition can generate radicals and gaseous byproducts that promote bubbles and voids if local temperatures become too high [19, 20]. Initiator loading also affects polymer network formation. Higher concentrations can accelerate conversion, but excessive radical generation can shorten kinetic chain length, increase termination reactions and produce heterogeneous, brittle networks with reduced mechanical performance [21, 22]. Preliminary samples prepared from the neat UV resin with TBPB showed severe warpage, yellowing, brittleness and premature fracture, preventing reliable tensile testing. A hybrid resin was therefore formulated by combining the thermal-curing infusion resin and UV-curable resin at a 50:50 ratio. This formulation preserved rapid UV response during deposition while reducing the degradation observed in TBPB-containing neat UV resin.

Figure 2a,b shows a sharp decrease in tensile properties of hybrid resin specimens as the TI content increases from 0–2%. Specimens were manufactured in a “brick and mortar” architecture to maximize shear-lag load transfer [15]. The tensile strength decreases from 68.52 ± 2.245 MPa to 49.92 ± 10.07 MPa with a large increase in variability demonstrating the highly unstable nature of TBPB. The slight increase in elastic modulus from 2.678 ± 0.107 GPa to 2.946 ± 0.535 GPa, indicates a stiffer but more brittle response due to increased TI concentration. FTIR analysis, shown in Fig. 2c,d, confirmed that thermal post-cure after UV exposure generally increased the degree of conversion, even though the UV-only condition used extended lamp exposure. For most TBPB concentrations, the UV + heat condition produced higher conversion than UV alone: at 0, 0.25, 0.50, 0.75, and 2 wt% TBPB, degree of cure increased from 63.96% to 67.83%, 57.37% to 60.67%, 56.48% to 65.84%, 54.18% to 64.23%, and 72.14% to 74.64%, respectively. The largest improvements occurred at 0.50 and 0.75 wt% TBPB, where thermal post-curing increased conversion by approximately 9–10%. These results show that thermal activation can continue polymerization after UV exposure, supporting the use of a dual UV/thermal cure strategy for carbon-fiber-rich regions where light penetration is limited. At higher concentrations between 1 and 2 wt%, the conversion response plateaued, consistent with excessive initiator loading increasing optical absorption or otherwise limiting UV-driven conversion [23].

Although FTIR confirmed that TBPB improved cure conversion, tensile testing of the printed carbon-fiber composite specimens showed that maximum conversion did not correspond to maximum mechanical performance. As shown in Fig. 3a,b, tensile strength increased from 276.199 ± 17.073 MPa without TI to 529.112 ± 40.144 MPa at 0.25 wt% TI, then decreased to 415.301 ± 53.683 MPa at 2 wt% TI. This non-monotonic response indicates that cure conversion alone is insufficient to identify the optimal formulation for fiber-reinforced specimens. The superior performance at 0.25 wt% TI likely reflects the best balance between improving cure in UV-shadowed carbon-fiber-rich regions and preserving matrix/interface quality. At low TI content, additional thermally generated radicals can increase residual cure and improve fiber–matrix load transfer. However, at higher TI contents, excessive radical generation can reduce kinetic chain length, increase termination and promote heterogeneous crosslinked networks [23–26]. Similar initiator-optimization studies have shown that mechanical properties can peak at intermediate initiator contents rather than at the highest conversion, supporting the conclusion that higher FTIR-measured conversion does not necessarily translate to higher composite strength [21, 24]. Therefore, 0.25 wt% TI is interpreted as the optimum for the printed composites because it provides sufficient thermal cure assistance while avoiding the network degradation, brittleness, and defect formation associated with higher thermal initiator loadings.

2.3. Failure and Damage

Examples of printed specimens are shown in Fig. 4a. Fractured specimens (Fig. 4b), show how tow pullout at discontinuity planes governs specimen failure. The fractured coupons exhibited extensive longitudinal splitting and partially intact tow bundles, indicating progressive tow–matrix debonding and pull-out prior to final rupture. Some specimens also showed transverse breaks across the coupon width, suggesting that final failure involved localized tow/tape fracture after interfacial damage and longitudinal splitting had developed. Delamination was not assigned as the primary mechanism because the observed damage was initiated by intralaminar interfacial fracture that resulted in tow pullout and fiber breakage through thickness.

Optically zoomed, and SEM images, shown in Fig. 4c-e, further show tow pullout zones, exposed tow surfaces, and local resin fracture. This indicates that tensile failure occurred through a mixed damage process involving matrix cracking, tow–matrix interfacial debonding, longitudinal tow splitting, and eventual tow rupture. Matrix yellowing observed in Fig. 4c indicates activation of the thermal initiator, likely accompanied by volatilization, which may lead to shrinkage and weaker interfacial bonding. Once a tow-tow interface was destroyed, the presence of long, partially intact pulled-out tow bundles suggests that load transfer between the discontinuous tow reinforcement and surrounding resin was insufficient to force uniform fiber fracture across the coupon cross-section. Thus, the failure morphology supports a progressive tow-level failure mechanism rather than simple brittle fracture of the composite.

2.4. Fiber Alignment and Volume Fraction Contributions

The primary drivers of composite strength and stiffness in the process are fiber orientation, fiber volume fraction, and degree of impregnation [36]. In the present process, alignment must be preserved at two length scales: the filament alignment within the carbon-fiber tow and the macro-scale alignment of each chopped tow segment after resin metering, impregnation, deposition and compaction. Unlike continuous-fiber placement, where axial tension constrains the reinforcement throughout deposition, each tow segment in this process becomes mechanically unconstrained after chopping. The deposition head must therefore prevent tow rotation, fanning and lateral spreading while the resin-wetted segment is transferred to the substrate.

Contour extraction from 200 deposited tow segments showed that 99% of measured tow orientations were within ± 2.58° of the programmed deposition direction. This narrow orientation distribution demonstrates that the integrated chopping, doctor-blade impregnation and deposition sequence preserves tow-level alignment despite the absence of continuous reinforcement tension. It also confirms that the process can generate aligned long discontinuous reinforcement directly during printing, rather than relying on a pre-aligned tape or preform [4].

Matrix burn-off and density measurements yielded a fiber volume fraction of 28 ± 2.2% and a void content of 8.2%. This fiber content is higher than typical commercially available fiber-reinforced additive-manufacturing filaments, which commonly contain 5–15% fiber, but remains below prepreg-based aerospace composites, which are often near 55% fiber volume fraction [2, 37]. The result is notable because the material is produced from dry tow with in situ resin metering and impregnation rather than from a pre-impregnated feedstock. At the same time, the measured void content identifies impregnation and compaction as the main opportunities for further improving mechanical performance.

Increasing fiber volume fraction in this architecture is not simply a matter of applying higher compaction pressure. In prepreg and automated fiber placement, compaction pressure can reduce porosity, drive resin flow or bleed-out and increase fiber packing because the reinforcement remains mechanically constrained [38, 39]. In the present fully discontinuous system, excessive compaction can split the tow bundle, fan out the cut tow ends and distort the intended rectangular tow cross-section, producing local misalignment. Conversely, insufficient resin flow or compaction can leave dry regions, incomplete tow impregnation and voids. Further increases in fiber volume fraction will therefore require coordinated control of doctor-blade resin metering, tow impregnation, compaction force and cure timing. Balancing fiber packing, tow shape retention and through-thickness impregnation remains a central processing challenge for aligned long discontinuous fiber additive manufacturing.

2.5. Manufacturing Capabilities and Design Implications

To assess manufacturing capability beyond flat coupons, the process was evaluated using geometries that require locally changing reinforcement paths, including honeycomb features, thin walls, an L-bracket and an open truss. Such structures are difficult to manufacture using conventional composite lattice approaches because they often require dedicated tooling, subcomponent assembly, joining or post-processing, which increases cycle time, material waste and manufacturing complexity [8–10]. The present end-effector architecture addresses this limitation by chopping, impregnating, aligning, depositing, compacting, and UV-fixing long discontinuous carbon-fiber tow segments immediately before placement. As a result, the material is deposited as discrete, resin-wetted tow segments rather than as a continuous or semi-continuous tape that must conform to the full toolpath.

This distinction is important for sharp bends and short-radius features. In continuous tape or tow placement, tight curvature produces inner- and outer-edge path-length mismatch, which can lead to tow pull-up, waviness, blistering, folding, or poor consolidation [39]. In contrast, the discontinuous-tow approach allows the reinforcement to follow locally varying paths by terminating and restarting tow segments along the programmed trajectory. This capability was demonstrated through representative honeycomb, thin-walled, L-bracket, and truss geometries, as shown in Fig. 5a–d.

Different reference structures were selected for the L-bracket and truss because the two geometries impose different manufacturing constraints. The L-bracket was compared with a vacuum-assisted resin transfer molding (VA-RTM) specimen because VA-RTM is an established out-of-autoclave process for composite structures. The truss was compared with a 3D-printed CF-PETG reference because its open, interconnected geometry is not readily produced by conventional composite molding without substantial tooling, assembly or post-processing. These comparisons are therefore used to evaluate geometry-level manufacturing capability and mass-normalized load-bearing response, rather than to isolate material performance alone.

The composite L-bracket achieved a sharp 90° corner, overcoming the geometric limitations typically associated with standard vacuum-assisted resin transfer molding. For comparison, the conventional composite L-bracket exhibited an inner radius of 5.6 mm and an outer radius of 8.0 mm, while continuous/semi-discontinuous tape placements are limited to in-plane circular paths with radii on the order of 35–75 cm [40]. Under compressive-flexural loading, the L-bracket produced in this work withstood a specific failure load of 0.085 kN/g, compared with 0.01627 kN/g for the conventionally produced specimen. This corresponds to an approximately 5.2-fold increase in specific load-bearing capacity. However, this comparison should be interpreted with consideration of differences in resin system, specimen thickness and fiber architecture.

The composite truss exhibited a specific compressive-flexural failure load of 0.0790 kN/g, compared with 0.0175 kN/g for the 3D-printed PETG-CF reference structure. This corresponds to an approximately 4.5-fold increase in specific load-bearing capacity.

Despite the improved load-bearing performance of both the truss and L-bracket, failure was governed by interfacial discontinuities rather than fiber rupture. As shown in Fig. 5e,f, damage initiated and propagated primarily along tow–tow interfaces, indicating that the reinforcing potential of the composite architecture was limited by local stress-transfer discontinuities. SEM observations in Fig. 5g,h further reveal through-thickness brittle resin fracture, evidenced by tow-shaped indentations in the fractured matrix. These fracture features suggest that cracking occurred around the embedded tows, allowing individual tows to delaminate from the surrounding resin. Within the intralayer direction, the tows split at the central joint, confirming that the joint acted as a

primary damage-initiation region where geometric constraint and stress transfer were most severe. Together, the macroscopic and microscopic fracture observations indicate a mixed failure mode involving brittle resin cracking, tow–matrix debonding, tow–tow interfacial separation, and localized tow splitting.

These results highlight a key trade-off in the current process: discontinuous tow placement enables sharp bends, corners, and lattice-like architectures, but the same discontinuities that provide geometric freedom also introduce local stress-transfer planes that can initiate damage. Future work will therefore focus on optimizing thin-wall toolpath generation to reduce localized failure and developing a variable-length chopping mechanism that introduces discontinuous reinforcement selectively only where it is mechanically or geometrically beneficial.

3. Discussion

Aligned long discontinuous fiber architectures offer a route to decouple local reinforcement direction from the steering-radius and edge-length constraints that limit continuous tow and tape placement. In this work, we demonstrate a direct additive manufacturing process that creates this architecture during deposition from dry continuous carbon-fiber tow and an uncured thermoset resin system. By integrating tow chopping, doctor-blade resin metering, in situ impregnation, compaction, and UV-triggered fixation within a compact robotic deposition head, the process eliminates separate tape making, suspension-based alignment, vacuum collection, and preform preparation.

The main manufacturing advantage is that reinforcement segmentation is introduced intentionally at the point of placement. Unlike continuous or semi-continuous tapes, which must deform through bends and corners, the deposited 50 mm tow segments can terminate and restart along prescribed trajectories. This enables sharp corners, short-radius features, thin walls, and open-cell geometries without forcing a continuous reinforcement path to accommodate severe inner- and outer-edge length mismatch. The demonstrated honeycomb, L-bracket, and truss structures therefore show how programmed tow-segment placement can expand the design space for aligned carbon-fiber composites.

The material results show that this geometric freedom can be achieved while maintaining high tow-level alignment and useful tensile performance. The printed composites achieved 99% tow alignment within ± 2.58°, 28 ± 2.2% fiber volume fraction, and 529.1 ± 40.1 MPa tensile strength at 0.25 wt% TBPB. The dual UV/thermal resin strategy is important because UV exposure stabilized the deposited tow path during printing, while thermal post-curing improved conversion in carbon-fiber-rich regions where light penetration was limited. However, strength did not increase monotonically with FTIR-measured conversion, indicating that the optimum formulation must balance cure completion with matrix toughness, interfacial quality, and tow-level load transfer.

The principal limitation of the current process is stress transfer across tow-level discontinuities. Fracture observations showed longitudinal splitting, tow pullout, tow–matrix debonding, and damage initiation at joints or discontinuity planes. These results indicate that the same discontinuities that enable geometric freedom can also introduce local failure sites. Future work should therefore focus on increasing fiber volume fraction, reducing void content, improving inter-tow bonding, and implementing variable-length chopping so that reinforcement discontinuities are introduced only where they are geometrically or mechanically beneficial.

4. Methods

Materials

Toray T700S carbon fiber tow was used as the reinforcement. A 5000 UV non-styrenated resin and System 4500 infusion epoxy resin were used as matrix materials. TBPB was used as the thermal initiator for the acrylate-based UV resin. Supplier-reported mechanical properties for the tow and resin systems are summarized in Table 1.

Table 1
Material properties of the carbon fiber tow and resin systems used in this study.

Material	Tensile strength (MPa)	Tensile modulus (GPa)	Flexural strength (MPa)	Flexural modulus (GPa)
T700S carbon fiber tow	4900	230	-	-
System 4500 infusion epoxy resin	75.6	3.36	130.6	3.64
5000 UV non-styrenated resin	103.4	4.14	171.7	4.39

FTIR characterization. Fourier transform infrared spectroscopy (FTIR, Thermo Fisher Nicolet iS20) was used to quantify degree of conversion (DC) by comparing uncured, UV-cured, and UV + thermally post-cured samples through the decrease in the aliphatic C = C absorbance relative to an invariant reference band. DC was calculated as

$$DC\,(\%) = \left[1 - \frac{(A_{1720}/A_{1635})_t}{(A_{1720}/A_{1635})_0}\right] \times 100$$

where $A_{C=C}$ and A_{ref} are the absorbances of the reactive and reference bands, respectively. Samples were cured under UV using the Uvitron SkyBeam 395 nm LED Spot Curing System and under heat up to 120° C to fully react the TI.

Constituent content and void fraction. Constituent content was measured by matrix ignition following ASTM D3171 using representative coupons sectioned from deposited laminates [41]. Fiber weight fraction and fiber volume fraction were calculated from the recovered reinforcement mass. Void volume fraction

was determined following ASTM D2734 by comparing measured composite density with the theoretical density obtained from the rule of mixtures using supplier-provided constituent densities [24].

Tow Alignment Measurement

High-resolution optical images of the deposited laminate surface were acquired under controlled lighting. Images were processed to segment individual tows, extract tow centerlines, and compute local tangent angles along each tow via contour extraction [42]. The resulting orientation distribution was reported relative to the intended deposition direction

Mechanical Testing

Tensile and flexural properties were measured using an INSTRON 68TM-50 with a 50 kN load cell according to ASTM D3039. Because standardized methods are not yet available for the targeted thin-walled structures, modified D3039 specimens with widths of 10–12 mm, corresponding to approximately one tow width, were used. 5 specimens were tested for each tensile sample set with a crosshead speed of 1 mm/min. For exemplar specimens, a modified compression test was performed utilizing 3-point bending fixtures.

Processability index. As no universally accepted metric exists for comparing the productivity, formability and flexibility of aligned discontinuous-fibre manufacturing routes, we defined a heuristic processability index for relative comparison. Guided by the processability–performance framework of Such *et al.* [4], each route was assigned four 1–5 scores describing directness (D), alignment-system simplicity (S), reproducibility (R) and cost (C), and the overall processability was calculated as

$$P = \frac{D + S + R + C}{4}.$$

The index was used only to rank processes relative to one another and was not treated as a measured material property. Tensile strengths for literature methods were taken from the comparative compilation, and the method proposed in this work was added using the measured strength from this study.

administration, funding acquisition, and writing—review and editing. All authors have read and agreed to the published version of the manuscript.

Declarations

Competing Interests

The authors declare the following competing interests: The University of Connecticut has filed U.S. Provisional Patent Application No. 64/049,520, titled “Robotic Additive Manufacturing System and End Effector for Aligned Long Discontinuous Fiber Composites,” related to the direct additive manufacturing process and deposition-head architecture described in this manuscript. Ji Ho Jeon, Minhajul Islam, Akshay Zaveri, Kisu Ok and Cheonghwa Lee are listed as inventors on the application. The application is pending. All other authors declare no competing interests.

Author Contributions

Akshay Zaveri: conceptualization, methodology, fabrication, investigation, formal analysis, data curation, visualization, writing—original draft preparation, and writing—review and editing. **Kisu Ok**: experimental testing and investigation. **Minhajul Islam**: experimental testing and investigation. **Cheonghwa Lee**: experimental testing and investigation. **Omar Bhatti**: experimental testing and investigation. **Jack Heroux**: experimental testing and investigation. **Jaeyoul Lee**: writing—review and editing. **Ji Ho Jeon**: conceptualization, supervision, project administration, funding acquisition, and writing—review and editing. All authors have read and agreed to the published version of the manuscript.

Acknowledgements

The authors gratefully acknowledge the School of Mechanical, Aerospace, and Manufacturing Engineering at the University of Connecticut for its support of this work, including access to research facilities, laboratory resources, and the institutional environment that enabled the manufacturing and characterization activities described in this study. The authors also thank Toray for supplying the T700S carbon-fiber tow used as the reinforcement material in this work.

Data availability

The data supporting the findings of this study are available within the Article and Supplementary Information. Additional raw tensile-testing data, FTIR spectra, tow-alignment images, constituent-content measurements and microscopy images are available from the corresponding author upon reasonable request.

References

1. Wang Q, Li T, Yang X, Wang K, Wang B, Ren M (2021) Prediction and compensation of process-induced distortions for L-shaped 3D woven composites. Compos Part Appl Sci Manuf 141:106211. https://doi.org/10.1016/j.compositesa.2020.106211

2. Zaveri A, Ok K, Lee C, Humfeld KD, Nielsen M, Ahn S-H et al (2025) Current Applications and Advancements in the Manufacturing of Discontinuous Fiber Composites. Int J Precis Eng Manuf-Green Technol. https://doi.org/10.1007/s40684-025-00815-z
3. Tsuji N, Springer GS, Hegedus I (1997) The Drapability of Aligned Discontinuous Fiber Composites. J Compos Mater 31:428–465. https://doi.org/10.1177/002199839703100501
4. Such M, Ward C, Potter K (2014) Aligned Discontinuous Fibre Composites: A Short History. J Multifunct Compos 2:155–168. https://doi.org/10.12783/issn.2168-4286/2/3/4/Such
5. Fu S (1996) Effects of fiber length and fiber orientation distributions on the tensile strength of short-fiber-reinforced polymers. Compos Sci Technol 56:1179–1190. https://doi.org/10.1016/S0266-3538(96)00072-3
6. Yu T, Zhang Z, Song S, Bai Y, Wu D (2019) Tensile and flexural behaviors of additively manufactured continuous carbon fiber-reinforced polymer composites. Compos Struct 225:111147. https://doi.org/10.1016/j.compstruct.2019.111147
7. Legenstein A, Füssel L, Heider D, Gillespie JW, Cender TA (2024) Stretch-steering of highly aligned discontinuous fiber tape with automated fiber placement. Compos Part B Eng 287:111801. https://doi.org/10.1016/j.compositesb.2024.111801
8. Hunt CJ, Morabito F, Grace C, Zhao Y, Woods BKS (2022) A review of composite lattice structures. Compos Struct 284:115120. https://doi.org/10.1016/j.compstruct.2021.115120
9. Zhang D, Tian X, Zhou Y, Wang Q, Yan W, Akmal Zia A et al (2023) Spatial 3D Printing of Continuous Fiber-Reinforced Composite Multilayer Truss Structures with Controllable Structural Performance. Polymers 15:4333. https://doi.org/10.3390/polym15214333
10. Liu B, Wang Y, Lou R, Yao Y, Chen X, Li H (2024) A new method of preparing lattice structures of continuous carbon fiber-reinforced thermoplastics. Compos Struct 329:117781. https://doi.org/10.1016/j.compstruct.2023.117781
11. Chopper Blades for 1171-A Chopper Gun In Stock (2026) Fibre Glast n.d. https://www.fibreglast.com/products/parts-for-1171-a-chopper-gun-1850
12. Gydesen E (1989) Doctor blade chamber device. WO1989007047A1
13. Deng K, Park S, Zhang C, Peng Y, Chadhauri A, Fu K (2024) Core-shell structured tow-pregs enabled additive manufacturing of continuously reinforced thermoset composites. Compos Part B Eng 271:111179. https://doi.org/10.1016/j.compositesb.2023.111179
14. Yourdkhani M, Dojan C, Ziaee M, Radosevich S Additive Manufacturing of Carbon Fiber-Reinforced Thermoset Composites via In-Situ Thermal Curing 2023. https://doi.org/10.21203/rs.3.rs-3397066/v1
15. Pimenta S, Robinson P (2014) An analytical shear-lag model for composites with 'brick-and-mortar' architecture considering non-linear matrix response and failure. Compos Sci Technol 104:111–124. https://doi.org/10.1016/j.compscitech.2014.09.001
16. Gupta A, Ogale AA (2002) Dual curing of carbon fiber reinforced photoresins for rapid prototyping. Polym Compos 23:1162–1170. https://doi.org/10.1002/pc.10509
17. Emtiaz SM, Shepherd N, Fuessel L, Deng K, Fu K, Advani SG (2026) Process-induced defects and their influence on inter-tow bond strength in dual-cure continuous fiber composite additive manufacturing. Compos Part B Eng 316:113572. https://doi.org/10.1016/j.compositesb.2026.113572
18. He M, Huang X, Huang Y, Zeng Z, Yang J (2012) Photoinduced redox initiation for fast polymerization of acrylaytes based on latent superbase and peroxides. Polymer 53:3172–3177. https://doi.org/10.1016/j.polymer.2012.05.031
19. Zhang D, Li Z, Jiang J, Ni L, Chen Z, Zhang D et al Thermal hazard assessment and free radical inhibition of decomposition of tert-butyl perbenzoate. Emerg Manag Sci Technol 2024;5. https://doi.org/10.48130/emst-0024-0029
20. Ziaee M, Yourdkhani M (2024) Bubble-Free Frontal Polymerization of Acrylates via Redox-Initiated Free Radical Polymerization. Polymers 16:2830. https://doi.org/10.3390/polym16192830
21. Przesławski G, Szcześniak K, Gajewski P, Marcinkowska A (2022) Influence of Initiator Concentration on the Polymerization Course of Methacrylate Bone Cement. Polymers 14:5005. https://doi.org/10.3390/polym14225005
22. Cheadle AMG, Maier E, Palin WM, Tomson PL, Poologasundarampillai G, Hadis MA (2025) The impact of modifying 3D printing parameters on mechanical strength and physical properties in vat photopolymerisation. Sci Rep 15:12592. https://doi.org/10.1038/s41598-025-97294-8
23. Van De Voorde KM, Kozawa SK, Mack JA, Thompson CB (2024) Influence of Cross-Linker Functionality and Photoinitiator Loading on Network Connectivity and Actuation in 3D-Printed Model Thermosets. ACS Appl Polym Mater 6:3918–3929. https://doi.org/10.1021/acsapm.3c03217
24. Wang K, Li B, Ni K, Li B, Wang Z (2021) Optimal photoinitiator concentration for light-cured dental resins. Polym Test 94:107039. https://doi.org/10.1016/j.polymertesting.2020.107039
25. Gong M, Zhang D, Zhang J, Li J, Chen X (2022) Optimization of initiator contents in room temperature polymerization of methyl methacrylate. Polym Polym Compos 30:09673911221143201. https://doi.org/10.1177/09673911221143201
26. 3.3 (2020) https://chem.libretexts.org/Bookshelves/Organic_Chemistry/Polymer_Chemistry_(Schaller)/03%3A_Kinetics_and_Thermodynamics_of_Polymerization/3 (accessed May 5, 2026)
27. Scholz M-S, Drinkwater BW, Trask RS (2014) Ultrasonic assembly of anisotropic short fibre reinforced composites. Ultrasonics 54:1015–1019. https://doi.org/10.1016/j.ultras.2013.12.001
28. Richter H, SINGLE FIBRE AND HYBRID COMPOSITES WITH ALIGNED DISCONTINUOUS, FIBRES IN POLYMER MATRIX (1980) Adv Compos Mater 387–398. https://doi.org/10.1016/B978-1-4832-8370-8.50033-4
29. Matthams TJ, Clyne TW (1999) Mechanical properties of long-fibre thermoplastic composites with laser drilled microperforations: 1. Effect of perforations in consolidated material. Compos Sci Technol 59:1169–1180. https://doi.org/10.1016/S0266-3538(98)00156-0
30. Kacir L, Narkis M, Ishai O (1978) Aligned short glass fibre/epoxy composites. Composites 9:89–92. https://doi.org/10.1016/0010-4361(78)90585-2

31. Goodine EK, Associates P, DiscoTex® Highly Formable Carbon Fiber Fabric n.d
32. Flemming T, Kress G, Flemming M (1996) A new aligned short-carbon-fiber-reinforced thermoplastic prepreg. Adv Compos Mater 5:151–159. https://doi.org/10.1163/156855196X00068
33. Ericson ML, Berglund LA (1993) Processing and mechanical properties of orientated preformed glass-mat-reinforced thermoplastics. Compos Sci Technol 49:121–130. https://doi.org/10.1016/0266-3538(93)90051-H
34. Edwards H, Evans NP, A METHOD FOR THE PRODUCTION OF HIGH QUALITY ALIGNED SHORT, FIBRE MATS AND THEIR COMPOSITES (1980) Adv Compos Mater 1620–1635. https://doi.org/10.1016/B978-1-4832-8370-8.50128-5
35. Yu H, Potter KD, Wisnom MR (2014) A novel manufacturing method for aligned discontinuous fibre composites (High Performance-Discontinuous Fibre method). Compos Part Appl Sci Manuf 65:175–185. https://doi.org/10.1016/j.compositesa.2014.06.005
36. Pimenta S, Pinho ST (2014) The influence of micromechanical properties and reinforcement architecture on the mechanical response of recycled composites. Compos Part Appl Sci Manuf 56:213–225. https://doi.org/10.1016/j.compositesa.2013.10.013
37. Manufacturing processes for composite materials and components for aerospace applications (2020) Polym Compos Aerosp Ind 59–81. https://doi.org/10.1016/B978-0-08-102679-3.00003-4
38. Jamora VC, Rauch V, Kravchenko SG, Kravchenko OG (2024) Effect of Resin Bleed Out on Compaction Behavior of the Fiber Tow Gap Region during Automated Fiber Placement Manufacturing. Polymers 16:31. https://doi.org/10.3390/polym16010031
39. Blackwell C, Simacek P, Crane R, Yarlagadda S, Advani SG (2023) A model for the autoclave consolidation of prepregs during manufacturing of complex curvature parts. Int J Mater Form 16:61. https://doi.org/10.1007/s12289-023-01784-x
40. Wrinkle Formation and Initial Defect Sensitivity of Steered Tow in Automated Fiber Placement (2026) n.d. https://www.mdpi.com/2504-477X/5/11/295
41. Standard Test Methods for Constituent Content of Composite Materials n (2026) d. https://store.astm.org/d3171-22.html
42. Suzuki S (1985) be K. Topological structural analysis of digitized binary images by border following. Comput Vis Graph Image Process ;30:32–46. https://doi.org/10.1016/0734-189X(85)90016-7

Figures

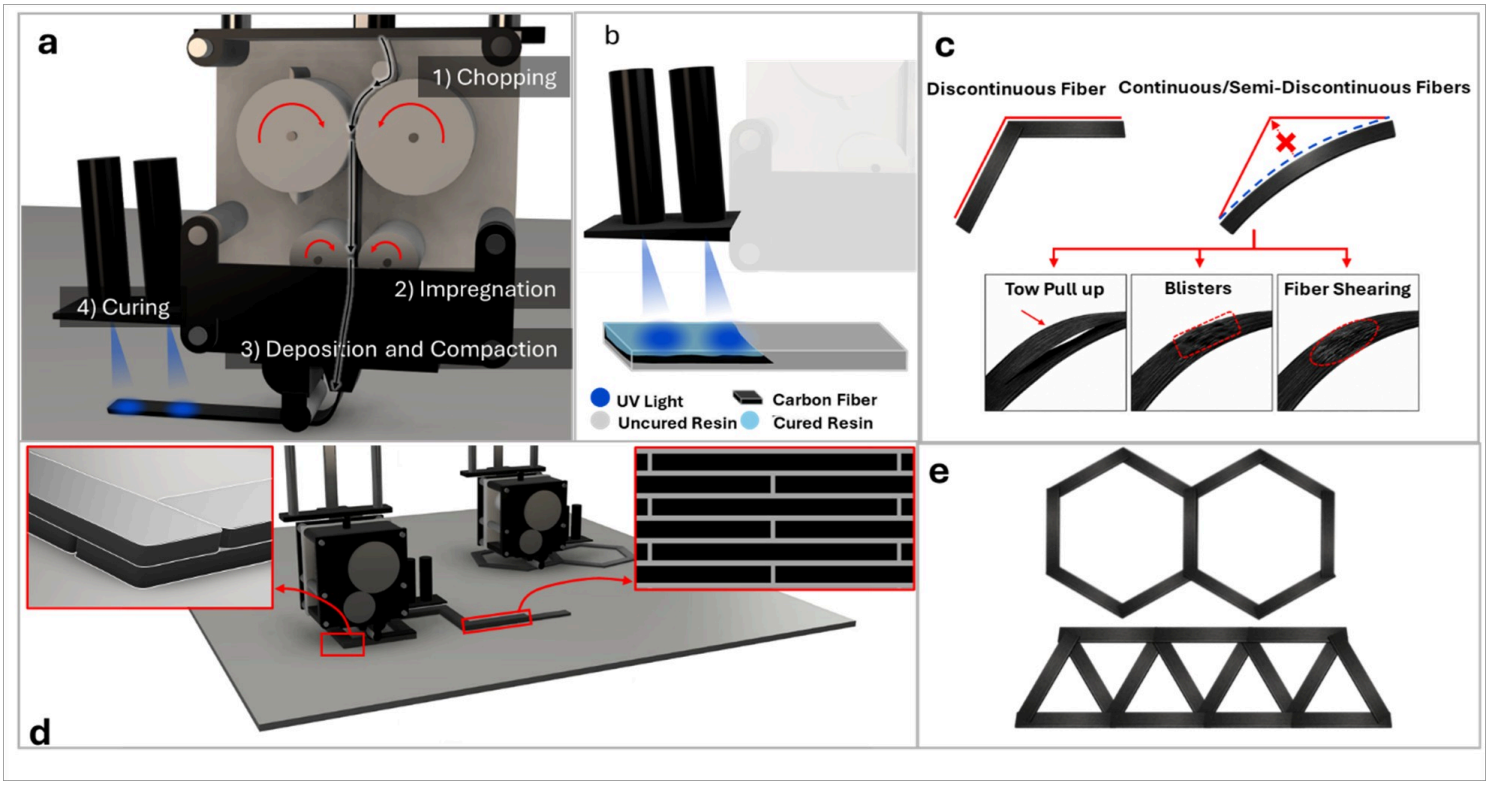


Figure 1

Compact end effector based Additive Manufacturing of Aligned Discontinuous Fiber Composites. (a) Schematic of the 4 sequential process steps. **(b)** Diagram of UV light penetration difficulties with “snap-cure”. **(c)** Detailed restrictions of continuous/semi-discontinuous fiber composites in complex geometries. **(d)** Example of additive manufacturing process with further detail of “brick-and-mortar” deposition architectures. **(e)** Representative geometries produced.

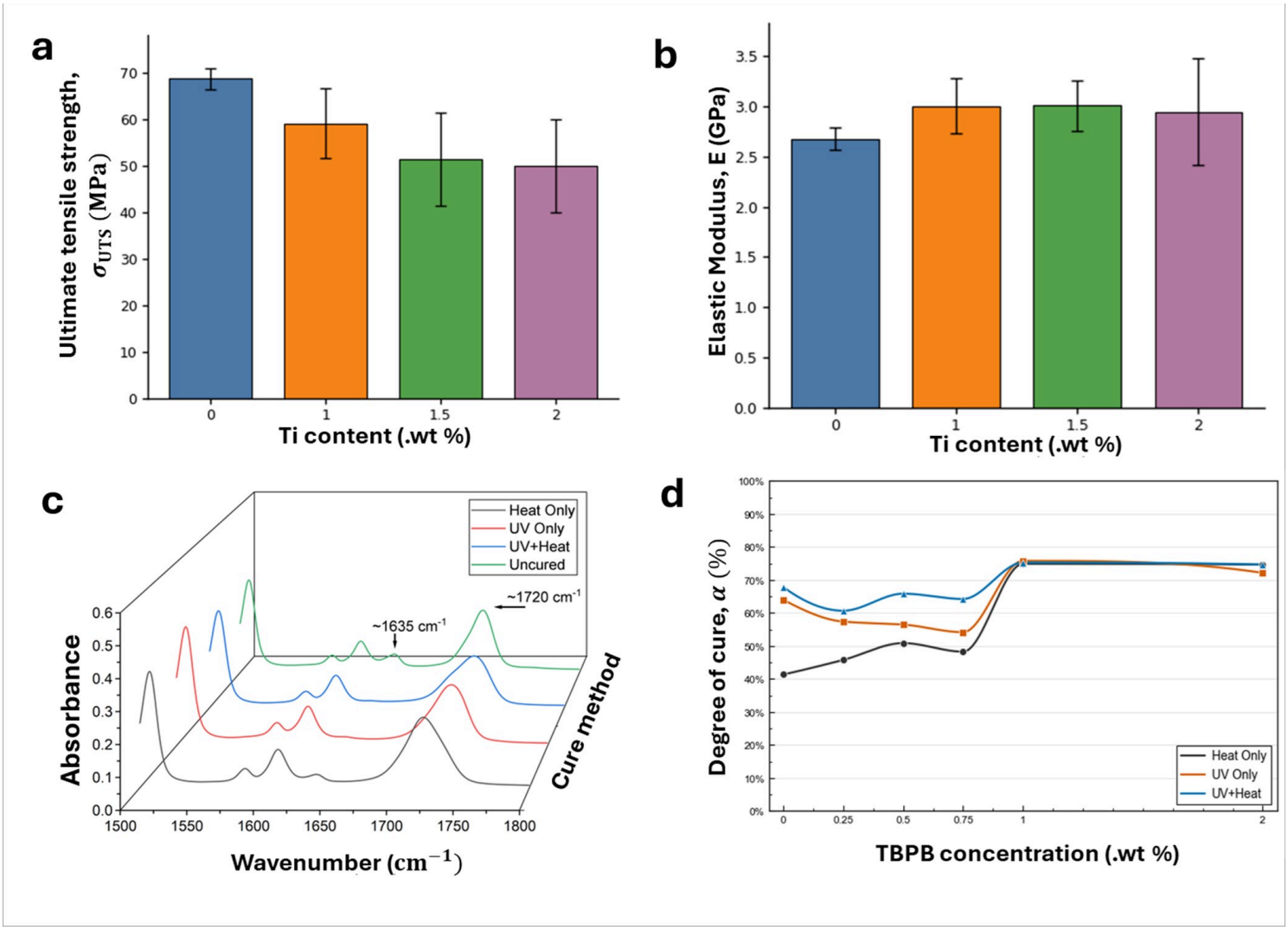


Figure 2

Mechanical and FTIR characterization of the dual UV/thermal resin system as a function of TBPB thermal initiator content. (a) Ultimate tensile strength of resin specimens with increasing TI content. **(b)** Elastic modulus of resin specimens with increasing TI content. **(c)**Representative FTIR spectra for the 0.25 wt% TBPB formulation under uncured, heat-only, UV-only, and UV + heat curing conditions. Degree of cure was calculated from the decrease in the aliphatic C=C absorbance near 1635 cm^{-1} relative to the carbonyl reference band near 1720 cm^{-1}. **(d)**FTIR-derived degree of cure for heat-only, UV-only, and UV + heat curing conditions across TBPB concentrations.

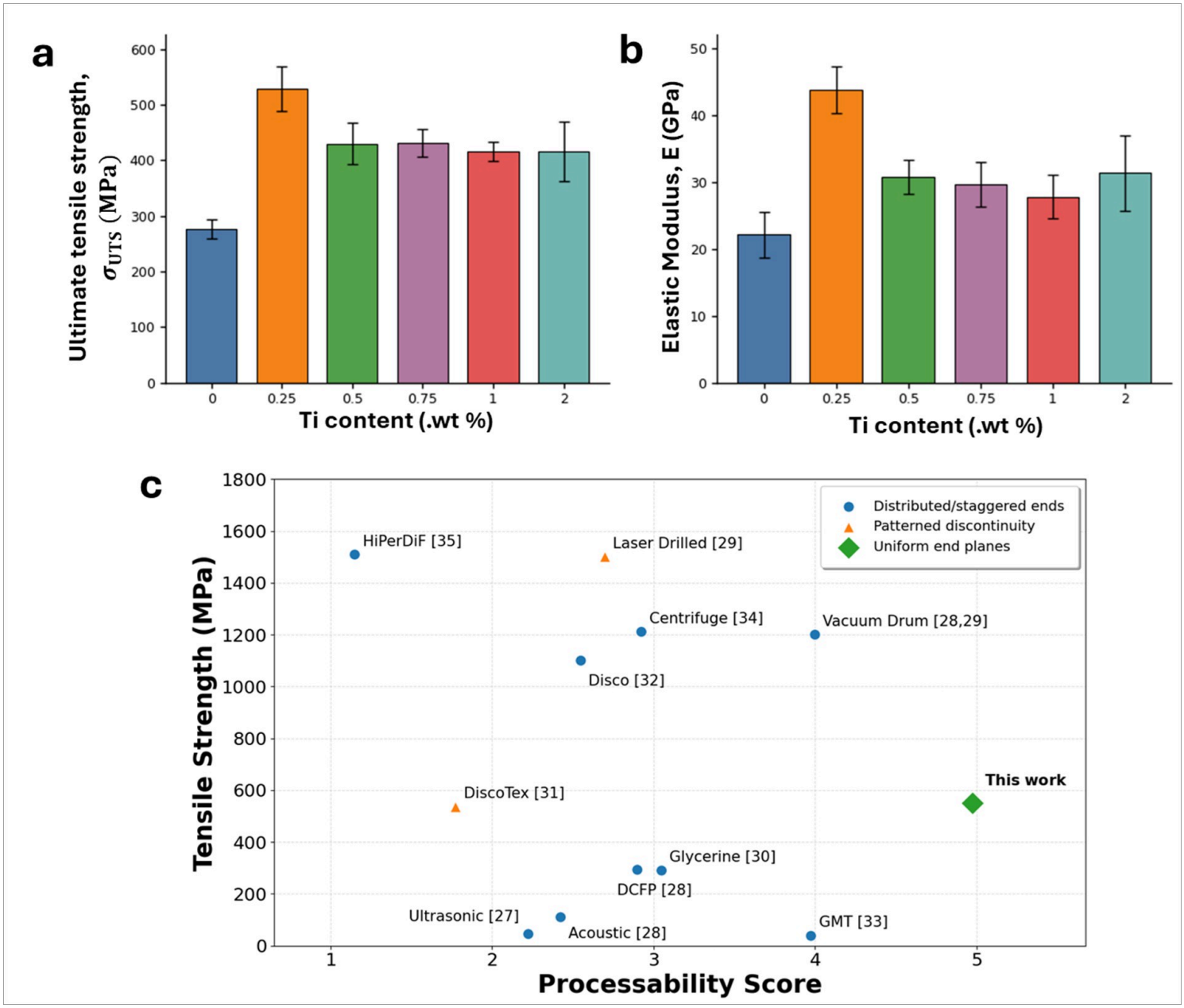


Figure 3

Mechanical characterization of additively manufactured Carbon Fiber samples and comparison with other works. **(a)**Ultimate tensile strength of resin specimens with increasing TI content. **(b)**Elastic modulus of resin specimens with increasing TI content. (c) Comparison of strength and processability with other works [27–35]

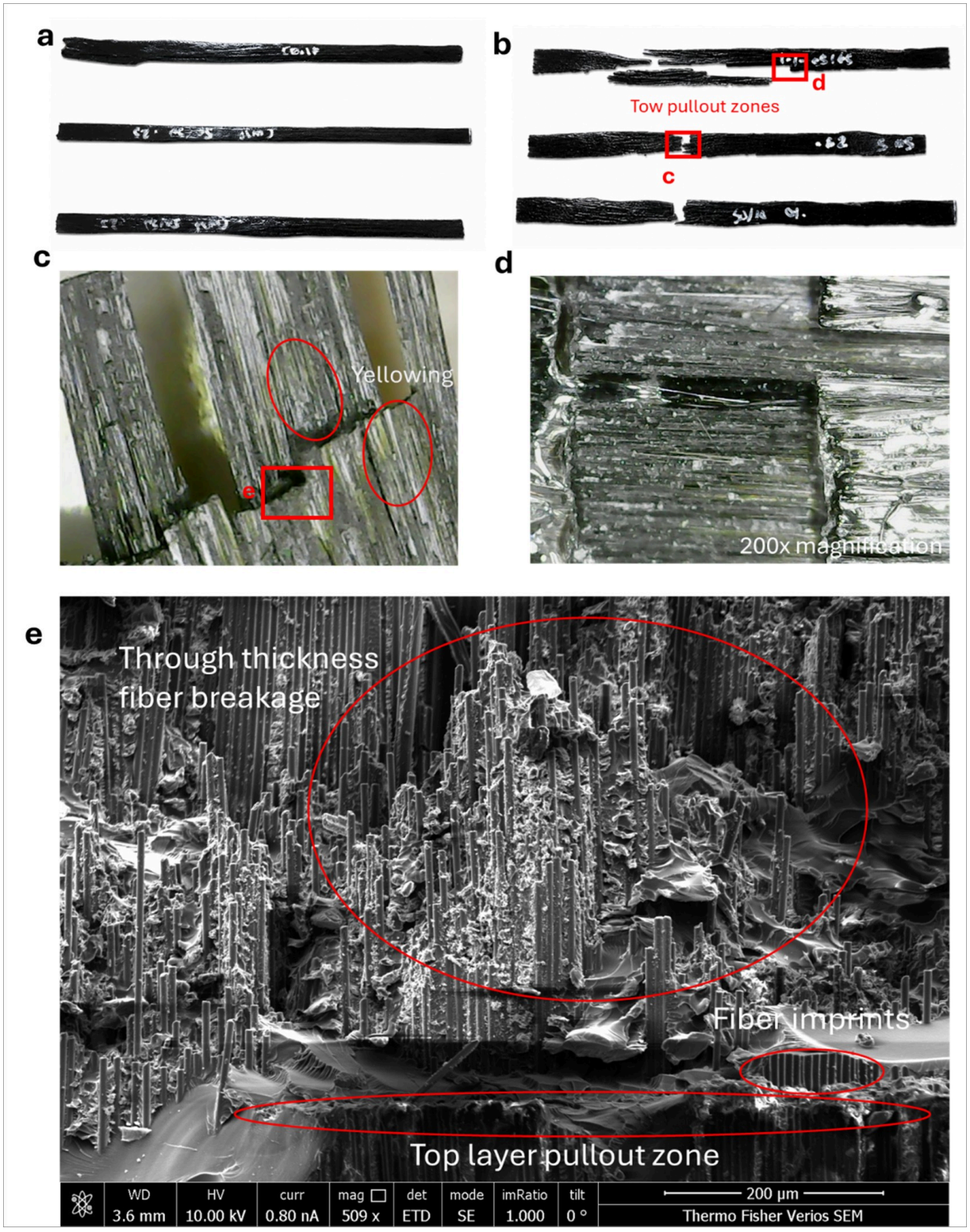


Figure 4

Failure morphology of printed discontinuous tow composite specimens. (a) Printed specimens before testing. (b) Fractured specimens showing tow pullout and discontinuity-plane failure. (c,d) Optical zoom images of fractured regions showing exposed tow surfaces, longitudinal splitting, tow–matrix debonding, pullout zones, and local resin fracture, indicating progressive tow-level failure followed by localized tow rupture. (e) SEM image showing fiber pullout zone and through thickness fiber breakage.

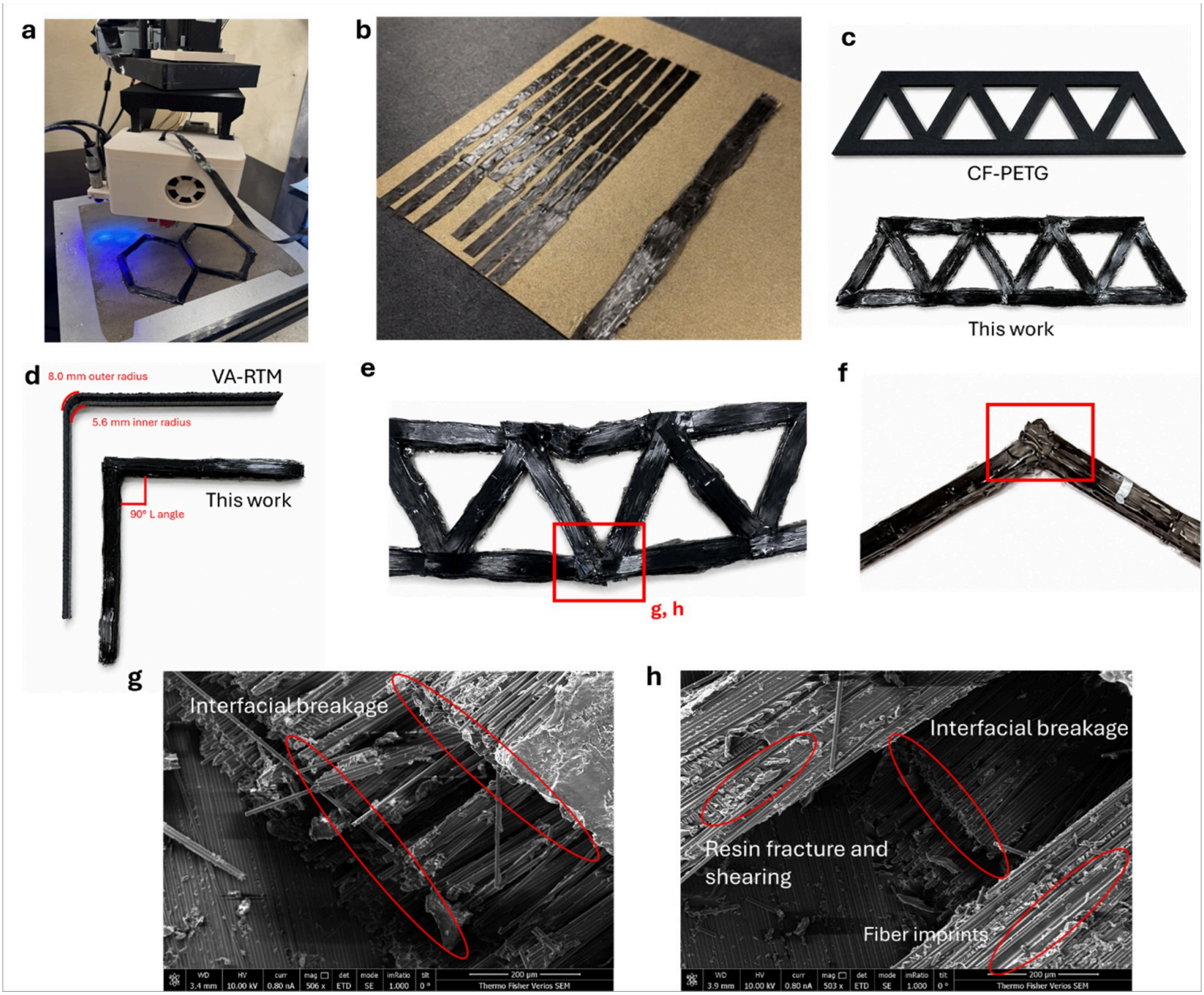


Figure 5

Fabrication, geometry, and failure characterization of the composite structures produced in this work. (a) Printing setup used to fabricate the continuous-fiber composite structures. **(b)**Example of alignment and sample creation. **(c)** Triangular truss fabricated in this work compared with a CF-PETG truss. **(d)**L-angle specimen fabricated in this work compared with a VA-RTM L-angle, showing the sharp 90° corner in this work relative to the larger inner and outer radii of the VA-RTM specimen. **(e)** Macroscopic fracture image of the triangular truss with the damaged joint region highlighted for SEM analysis. **(f)** Macroscopic fracture image of the L-angle specimen with the corner damage region highlighted. **(g, h)** SEM image of the fractured truss joint showing interfacial breakage between fiber bundles and resin.

Supplementary Files

This is a list of supplementary files associated with this preprint. Click to download.

- Video1.mp4
- Video2.mp4
- Video3.mp4
- Video4.mp4
- SupplementaryData.docx